

Tuning the Magnetic Properties of the CrMnFeCoNi Cantor Alloy

Timothy A. Elmslie^a, Jacob Startt^b, Yang Yang^c, Sujeily Soto-Medina^c, Emma Zappala^d,
Mark W. Meisel^{a,c}, Michele V. Manuel^c, Benjamin A. Frandsen^d, Rémi Dingreville^b, James J. Hamlin^a

^aDepartment of Physics, University of Florida, Gainesville, FL 32611-8440, USA

^bCenter for Integrated Nanotechnologies, Sandia National Laboratories, Albuquerque, NM, 87185, USA

^cDepartment of Materials Science and Engineering, University of Florida, Gainesville, FL 32611-6400, USA

^dDepartment of Physics and Astronomy, Brigham Young University, Provo, UT 84602, USA

^eNational High Magnetic Field Laboratory, University of Florida, Gainesville, Florida 32611-8440, USA

Abstract

Magnetic properties of more than twenty Cantor alloy samples of varying composition were investigated over a temperature range of 5 K to 300 K and in fields of up to 70 kOe using magnetometry and muon spin relaxation. Two transitions are identified: a spin-glass-like transition that appears between 55 K and 190 K depending on composition, and a ferrimagnetic transition that occurs at approximately 43 K in multiple samples with widely varying compositions. The magnetic signatures at 43 K are remarkably insensitive to chemical composition. A modified Curie-Weiss model was used to fit the susceptibility data and to extract the net effective magnetic moment for each sample. The resulting values for the net effective moment were either diminished with increasing Cr or Mn concentrations or enhanced with decreasing Fe, Co, or Ni concentrations. Beyond a sufficiently large effective moment, the magnetic ground state transitions from ferrimagnetism to ferromagnetism. The effective magnetic moments, together with the corresponding compositions, are used in a global linear regression analysis to extract element-specific effective magnetic moments, which are compared to the values obtained by ab-initio based density functional theory (DFT) calculations. These moments provide the information necessary to controllably tune the magnetic properties of Cantor alloy variants.

Keywords: Cantor alloy, high entropy alloy, magnetism

1. Introduction

Work on high-entropy alloys began in the early 2000s with Cantor, Kim and Warren [1]. However, the name “Cantor alloy” did not come about until a 2004 study by Yeh *et al.* [2] coined the term. Since that time, high-entropy alloys have garnered increasing attention for opening a massive number of yet-unexplored alloy systems for investigation. Already, studies have found a number of high-entropy alloys with interesting and potentially useful properties such as high hardness and resistance to anneal softening [2], shape memory effects [3, 4], and superconductivity [5].

Much work has been done regarding the mechanical properties of Cantor alloys [6–11], as well as the magnetic properties of similar compounds [12–23], and previous studies on the equiatomic Cantor alloy specifically have revealed the presence of two magnetic transitions. The higher temperature transition occurs at approximately 85 K, and has been identified as spin-glass-like through μ SR studies [24]. At approximately 43 K, the material transitions again, this time into a ferrimagnetic state, as determined by density functional theory (DFT) simulations and experimental analysis of the magnetic entropy [24]. Despite the small size of the ferrimagnetic transition, prior work has suggested that it is not due to an impurity phase [24]. Other studies have observed notable differences in the size and temperature

of these transitions, likely due to the significant processing dependence of the Cantor alloy [25–27]. Not only are the magnetic properties of the alloy highly sensitive to annealing and cold-working [28–30], high-temperature anneals do not eliminate the effects of cold-working. Analysis which combined modified Curie-Weiss fitting, specific heat measurements, DFT calculations and Hall measurements has also revealed a large Stoner enhancement factor [24].

Additionally, few papers have reported the magnetic properties of four-element combinations of the Cantor alloy, but the nature of the magnetic states has not been universally established. For example, Kao *et al.* [14] and Lucas *et al.* [15] both investigated CrFeCoNi, but Lucas *et al.* state that the compound is paramagnetic at low temperature, while Kao *et al.* claim that it is ferromagnetic. In this work, a number of four-element compounds were synthesized and measured alongside numerous five-element compounds with varying compositions in order to resolve these issues.

Our measurements of magnetic susceptibility on more than twenty Cantor alloy samples with varying compositions reveal that increasing the relative amount of ferromagnetic elements, such as Fe, enhances the overall magnetization, while larger quantities of antiferromagnetic elements decrease the magnetization. This observation is consistent with previous Cantor alloy investigations, which reported Fe, Co, and Ni tend to align ferromagnetically while Cr and Mn are typically antiferromagnetic [23, 24, 26]. Herein, these trends are quantified

Email address: jhamlin@ufl.edu (James J. Hamlin)

by least squares analysis performed using effective moments of each of the measured samples, revealing that element-specific magnetic moments can be estimated for samples that are close to the equiatomic composition. However, the magnetic properties change when the effective moment becomes sufficiently large due to a lack of antiferromagnetic elements or a relative abundance of ferromagnetic ones. At this point, the compound becomes ferromagnetic, rather than ferrimagnetic at low temperature as evidenced by muon spin-relaxation studies on select samples in the Mn series. Our experimental results, combined with ab-initio based density functional theory (DFT) calculations, provide a complete picture of the compositional dependence of the magnetic properties of the Cantor alloy system. The work highlights the great promise of similar regression analysis methods applied to several chemically substituted alloy samples to provide insights into elemental specific contributions to properties in other high-entropy materials.

2. Methods

This section describes the details of the various experimental and computational methods that were employed in this work, including the sample synthesis, magnetic and structural characterization, and density functional theory calculations.

2.1. Synthesis

Samples were synthesized by combining stoichiometric quantities of elemental Cr, Mn, Fe, Co, and Ni in an Edmund Bühler MAM-1 Compact Arc Melter. Chromium, manganese, iron, and nickel were sourced from Alfa Aesar, while cobalt was purchased from Cerac. The chromium used for synthesis was 99.995% pure, while the cobalt was 99.5% pure. All other elements were 99.95% pure. Each sample was melted five times, flipping it over between each melt to improve sample homogeneity. Following synthesis, samples were sealed in quartz tubes in Ar atmosphere and annealed at 1100 °C for six days, then quenched in water before measurement. However, the samples consisting of 25% of one element and 18.75% of each other element (25% samples) were annealed first for six days at 1080 °C and then again at 1100 °C, quenching in water following each anneal.

2.2. Sample Nomenclature

To simplify the process of investigating varying compositions, in each sample, the amount of only one element was adjusted, and all other elements remained in an equiatomic ratio according to the atomic ratios, $A_x[BCDE]_{100-x}$. For example, when adjusting the amount of Mn, sample compositions would follow the pattern $Mn_x(CrFeCoNi)_{100-x}$. This practice permits a simplified notation, listing only the element with an adjusted quantity and the percentage of that element present in the alloy. From that information alone, the relative proportion of other elements can then be inferred. For example, “Cr₂₂” is used instead of writing “Cr₂₂(MnFeCoNi)₇₈”, and a sample with composition CrFeCoNi is represented by the abbreviation “Mn₀.” This convention is used from this point onward in this work.

Samples with an equal proportion of each element (equiatomic) are listed as “Equi.”

2.3. Magnetic Characterizations

Magnetization and susceptibility measurements were performed using a Quantum Design Magnetic Property Measurement System (MPMS). Small pieces ranging from a few milligrams to a few hundred milligrams (typically ≈ 50 mg), were cut from larger samples using an Allied 3000 low speed saw to minimize unintentional working of the samples. Each sample was secured in a gel capsule inside a plastic straw for measurement.

Muon spin spectroscopy measurements (μ SR) were conducted at TRIUMF Laboratory in Vancouver, Canada using the LAMPF spectrometer on the M20D beamline. The μ SR technique utilizes the asymmetric decay of initially spin-polarized positive muons into positrons to probe the magnetic properties of the sample [31]. Specifically, μ SR is uniquely sensitive to the volume fraction of different magnetic and nonmagnetic phases, which is important for potentially inhomogeneous systems such as magnetic alloys. The experimentally measured quantity is the time-dependent asymmetry, $a(t)$, which is determined from the difference in positron events between two detectors placed on opposite sides of the sample. The asymmetry is proportional to the component of the net muon spin polarization along the axis connecting the two detectors. Information about the local magnetic field distribution can be inferred from the behavior of $a(t)$ as a function of temperature and applied magnetic field. Additional details about our experimental configuration are described elsewhere [24], and the open source program BEAMS [32] was used for data analysis.

2.4. Structural and Composition Characterizations

The crystal structure of the sample was investigated using a Panalytical Xpert X-Ray Diffraction (XRD) with a Cu K-alpha radiation source at a voltage of 45 kV and current of 40 mA in the 2θ range of 30-100°. The powder samples were prepared using a steel file. The microstructure of the sample was characterized using a Tescan MIR3 scanning electron microscope (SEM) at 20 kV. The epoxy-mounted sample was first ground using a series of SiC paper at steps of 600 grit, 800 grit, and 1200 grit, then further polished using alcohol-based lubricant and diamond paste in the sequence of 6 μ m, 3 μ m, and 1 μ m. The sample surface was master polished using 0.05 μ m water-free colloidal silica suspension. The chemical composition of the sample was determined using an equipped energy-dispersive X-ray (EDX) detector.

2.5. Computational methods

Ab-initio based density functional theory (DFT) calculations were performed in parallel to experimental investigation to study the net moment behavior of the low temperature ferrimagnetic phase as a function of composition. All DFT calculations were performed in the spin-collinear polarized state using the Vienna Ab-initio Simulation Package (VASP) [33–35]. Electronic wavefunctions were thus modeled using plane-waves while the interaction between the frozen core states and

valence states was handled according to the projector-augmented wave (PAW) formalism [36, 37]. Exchange and correlation was treated according to the generalized gradient approximation as parameterized by Perdew, Burke, and Ernzerhof (PBE) [38].

The modeled Cantor compositions were selected according to the same convention used in the experimental analysis, such that only one element was varied at time, according to $A_x[\text{BCDE}]_{100-x}$, resulting in five separate series of simulations (*i.e.*, one for each species). Within each series, four compositions were modeled (*i.e.*, $x = 10, 20, 30, 40$). The alloys were modeled using supercells containing 108 atoms, constructed as $3 \times 3 \times 3$ cubic multiplications of the conventional 4 atom FCC unit cell. Three separate supercells, each with a newly randomized ordering of the atoms among the lattice sites, were constructed for each composition modeled. Thus, any reported properties represent the average of the three random solution supercells at each composition.

For all calculations, a $5 \times 5 \times 5$ gamma-centered k-point mesh, along with a plane-wave energy cutoff of 400 eV and a Gaussian smearing width of 0.01 eV was found to sufficiently minimize fluctuations in the total energy and magnetic moments. The minimization threshold of the total energy with respect to the electronic convergence was set to 1.0×10^{-6} eV, while ionic convergence threshold was met when forces on all atoms fell below 20×10^{-3} eV \AA^{-1} .

3. Results

In this section, the results of magnetization as a function of temperature and magnetic field are described along with the low temperature μSR data. These experimental findings are analyzed and contrasted with the DFT work in the next section.

3.1. Magnetization

In Fig. 1, results of susceptibility versus temperature measurements are presented on the left side, while magnetization versus field results are shown on the right. Each row displays a collection of samples, grouped according to the elemental concentration being adjusted. Due to their strong magnetic response, most of the $x = 0$ samples are not included in this figure, with Fe_0 as an exception, so the composition dependence of the trends and features of the $x > 0$ data can be more easily compared. The Cr_0 and Mn_0 data sets are plotted in Fig. 2.

Three striking features are identified in the plots shown in Fig. 1. Firstly, a spin-glass-like transition (T_2), marked by a peak [24, 26], occurs at high temperatures, which varies widely depending on composition. This feature is most apparent in the Fe_{30} dataset at about 67 K, Fig. 1E. Secondly, a step-like feature (T_1) appears in many datasets, marking a ferrimagnetic transition [24], as clearly present in the Mn_{25} susceptibility data, Fig. 1C. In all samples in which it appears, the T_1 feature occurs at 43(1) K, and although this robustness might be considered as a fingerprint of an impurity phase, prior work has established this transition to be intrinsic to the Cantor alloy [24]. Lastly, another feature (T^*) occurs in several samples at approximately 18 K and is most obvious in the Mn_{25} data, Fig. 1C. The nature

of the T^* feature is unclear, but may be the result of differences in processing. The $x = 25$ samples were annealed and quenched twice, once at 1080 K and then at 1100 K, whereas other samples in which T^* appears were annealed and subsequently quenched in the same quartz tube along with several more pieces (up to as many as five), which may have resulted in a slower quench.

The magnetization versus field data along the right side of Fig. 1 shows that even at fields of up to 70 kOe, magnetization remains a small fraction of a Bohr magneton. For example, the Fe_{25} sample reaches approximately $0.03 \mu_B \text{ atom}^{-1}$, much smaller than the Hund’s-rule-predicted effective moments for the constituent elements, which is typically a few $\mu_B \text{ atom}^{-1}$ [39]. Thus, near-equiatom compositions of the Cantor alloy are far from magnetic saturation even at 70 kOe. Even in Mn_{10} , which extends beyond the limits of the y-axis (Fig. 1D), the magnetization reaches only $0.08 \mu_B \text{ atom}^{-1}$ at 70 kOe. One trend visible in Fig. 1 is that hysteresis increases as susceptibility increases, perhaps indicating the presence of ferromagnetic regions within the material.

The plots of Fig. 1 also reveal that susceptibility increases with greater proportions of ferromagnetic elements Fe, Co, or Ni. On the other hand, increasing the relative amount of antiferromagnetic elements Cr or Mn decreases the susceptibility. At sufficiently low concentrations of Cr or Mn, the magnetic properties change significantly, resulting in larger saturation magnetization and susceptibility. Consequently, Cr_0 and Mn_0 data are excluded from Fig. 1 and are instead presented in Fig. 2. The Cr_0 sample reaches susceptibility values of approximately $9.1 \text{ emu mol}_{\text{atom}}^{-1} \text{ Oe}^{-1}$, much larger than the susceptibility maximum of, for example, Mn_{25} of about $6.8 \times 10^{-3} \text{ emu mol}_{\text{atom}}^{-1} \text{ Oe}^{-1}$. Although the susceptibility and saturation magnetization of the Cr_0 and Mn_0 samples are orders of magnitude larger than those shown in Fig. 1, they are still lower than effective moments predicted by Hund’s rule [39]. These Cr_0 and Mn_0 samples also possess a single ferromagnetic transition, compared to the ferrimagnetic and spin-glass-like transition of the near-equiatom samples.

Transition temperatures for each measured sample are summarized in Table 1. The positions of the lower temperature (“step-like”) transitions were determined by local minima of the first derivative, while the critical temperature of the higher temperature transitions are located at the peak in the magnetic susceptibility. In several of the iron samples, the ferrimagnetic transition is either absent or too small to detect, and the spin-glass/antiferromagnetic transition is not visible in the ferromagnetic (Cr_0 and Mn_0) or nearly ferromagnetic (Mn_{10}) samples.

3.2. Muon Spin Spectroscopy

μSR measurements of Mn_0 and Mn_{30} alloys were conducted to evaluate the magnetic homogeneity and confirm the magnetization results. Representative $a(t)$ asymmetry spectra collected in zero applied magnetic field (ZF) are shown in Fig. 3(a) and (b) for Mn_0 and Mn_{30} , respectively. For both samples, the gentle relaxation of the asymmetry at high temperature becomes more rapid as the temperature is lowered toward the transition due to critical slowing down of spin fluctuations. Be-

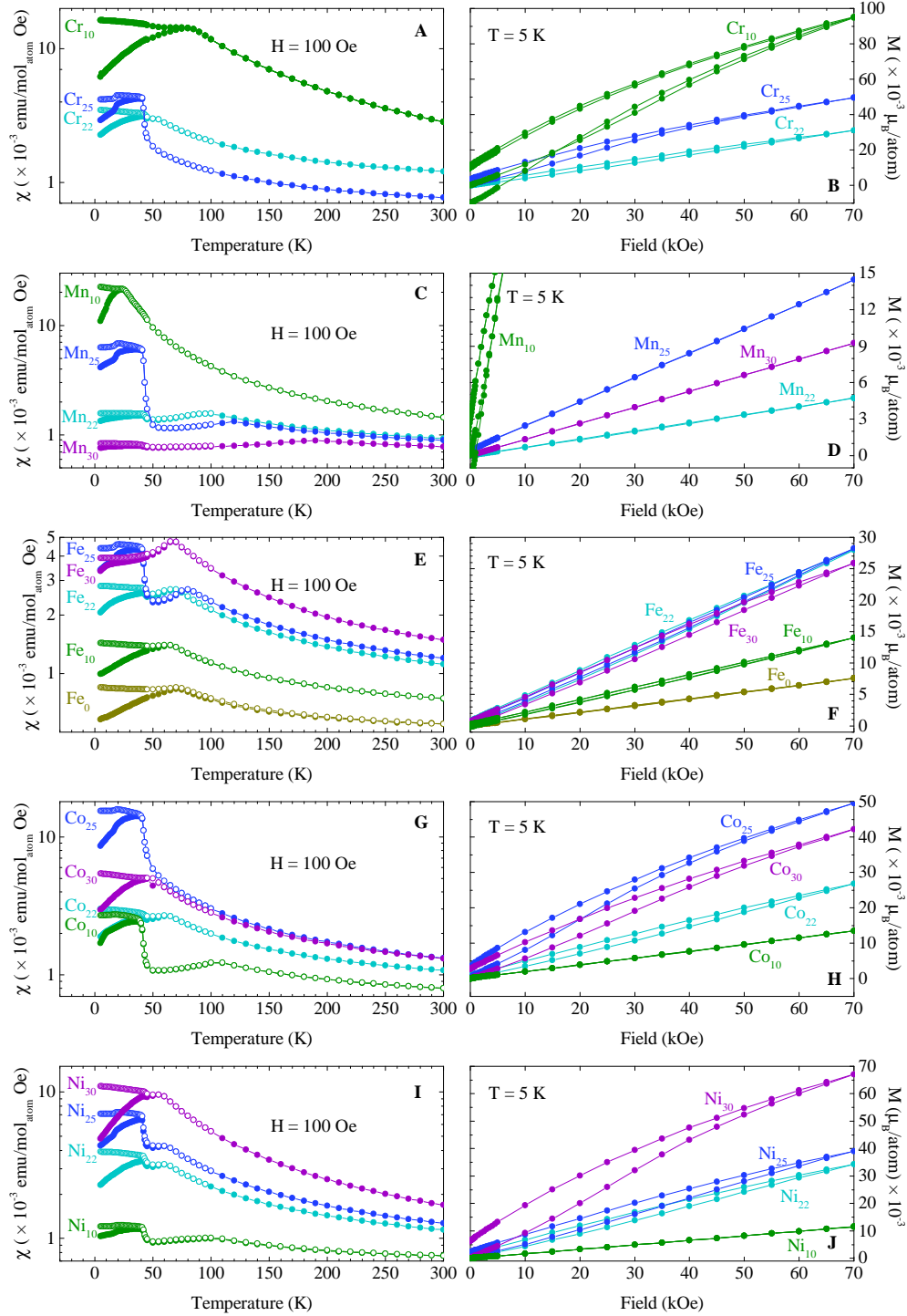


Figure 1. Susceptibility and magnetization data for Cantor alloys of varying compositions. Panels on the left show susceptibility versus temperature on a logarithmic scale, while those on the right show magnetization as a function of magnetic field. In the susceptibility plots, solid circles represent zero-field cooled (ZFC) data, which were measured after cooling down in zero field. Open circles represent field-cooled warming (FCW) data, which were collected after cooling down in an applied field of 70 kOe. Each row displays a different set of compounds: (A)-(B) Cr-varied compositions, (C)-(D) Mn-varied compositions, (E)-(F) Fe-varied compositions, (G)-(H) Co-varied compositions, and (I)-(J) Ni-varied compositions. Section 2.1.2 describes the sample nomenclature. Certain curves such as Mn_{10} and Fe_{30} display only one feature. In these cases, the feature is identified as T_1 or T_2 depending on its shape, with T_1 being step-like and T_2 being a peak.

Composition	T_1 (K)	T_2 (K)	$\chi_0(\times 10^{-3} \text{emu mol}_{\text{atom}}^{-1} \text{Oe}^{-1})$	$p_{\text{eff}} (\mu_B)$	θ (K)
Equi ([§])	44	82	5.57(4)	0.98(10)	-8.9(8)
Cr ₀ (^{*†})	180	-	-	-	-
Cr ₁₀ ([*])	44	80	-10.1(5)	2.9(4)	15.6(9)
Cr ₂₂	44	55	7.761(16)	1.02(6)	-5.10(21)
Cr ₂₅	42	-	5.287(22)	0.77(7)	-9.6(5)
Mn ₀ (^{*†})	75 [‡]	-	-	-	-
Mn ₁₀	44	-	1.75(23)	1.67(19)	13.3(5)
Mn ₂₂	43	100	5.640(27)	0.95(9)	-11.6(9)
Mn ₂₅	42	120	5.608(28)	0.91(10)	-17(1)
Mn ₃₀	43	190 [‡]	6.07(27)	0.6(3)	14(29)
Fe ₀	-	70	4.667(23)	0.44(7)	10(2)
Fe ₁₀	-	65	5.281(20)	0.73(7)	-11.7(8)
Fe ₂₂	43	67	5.868(9)	1.13(5)	-5.20(14)
Fe ₂₅	42	80	5.80(3)	1.23(10)	-7.2(5)
Fe ₃₀	-	67	5.09(14)	1.51(18)	3(1)
Co ₁₀	42	105	5.264(16)	0.83(7)	-13.6(7)
Co ₂₂	43	62	6.079(13)	1.07(6)	-4.37(19)
Co ₂₅	42	-	4.93(5)	1.39(10)	3.4(3)
Co ₃₀	-	50	5.60(3)	1.34(8)	0.15(21)
Ni ₁₀	43	100	6.35(3)	0.53(10)	9(3)
Ni ₂₂	43	60	5.653(17)	1.18(6)	-4.20(19)
Ni ₂₅	42	60	4.44(3)	1.40(9)	-1.27(24)
Ni ₃₀	44	55	0.05(17)	1.96(19)	10.0(6)

Table 1. Transition temperatures and modified Curie-Weiss fitting parameters of each measured alloy. [§]Data on the equiatomic compound were obtained by averaging values from four samples. ^{*}Asterisks mark samples that could not be accurately fit by the modified Curie-Weiss equation or produced unphysical results from fitting. [†]Daggers indicate samples which become ferromagnetic below the T_1 transition temperature, as opposed to the ferrimagnetic state assumed by other samples. [‡]Double daggers indicate transition temperatures that were confirmed via muon spin-relaxation measurements.

tween 77 – 80 K for Mn₀ and 175 – 185 K for Mn₃₀, the initial asymmetry value at $t = 0$ drops to approximately 1/3 of its high-temperature value, signifying the onset of static magnetism [31]. These temperatures agree well with $T_1 = 75$ K for Mn₀ and $T_2 = 190$ K for Mn₃₀ given in Table 1. The narrow temperature range in which the initial asymmetry drops demonstrates that the magnetic transition is sharp and uniform throughout the entire volume of the sample, *confirming that the non-stoichiometric alloys are similarly magnetically homogeneous as the equiatomic alloy* [24]. The uniform magnetic behavior of each sample is further illustrated in Fig. 3(c), where the initial asymmetry plotted as a function of temperature shows an abrupt step at the transition. The initial asymmetry was determined by fitting the generalized exponential function $a(t) = a_0 \exp(-\lambda t)^\beta$ to the spectra, as was done previously [24]. It is noteworthy that a characteristic Kubo-Toyabe relaxation pattern [40] is observed for Mn₀ within the first ~ 100 ns of the spectra below the transition, but is not visible on the time scale used in Fig. 3(a), in contrast to Mn₃₀ and the equiatomic al-

loy [24], indicative of subtle composition-dependent changes of the internal magnetic field distribution at the muon stopping sites.

Finally, Fig. 3(d) displays the temperature-dependent relaxation rate λ_{LF} of the long-time asymmetry for data collected in an applied longitudinal field (LF) of 1 kOe (not shown), which is a sensitive probe of spin dynamics. The values of λ_{LF} were determined from generalized exponential fits to the LF asymmetry spectra. Mn₀ shows a low, broad peak in λ_{LF} centered around 90 K (slightly above the transition temperature in ZF), while Mn₃₀ shows a much higher and sharper peak centered around 180 K. These results point to differences in the spin dynamics of the two samples, with critical behavior being suppressed in Mn₀ and preserved in Mn₃₀. A more detailed theoretical investigation of the microscopic magnetic behavior of Cantor alloys with various Mn-compositions could help explain these differences in the ZF and LF data of the Mn₀ and Mn₃₀ samples.

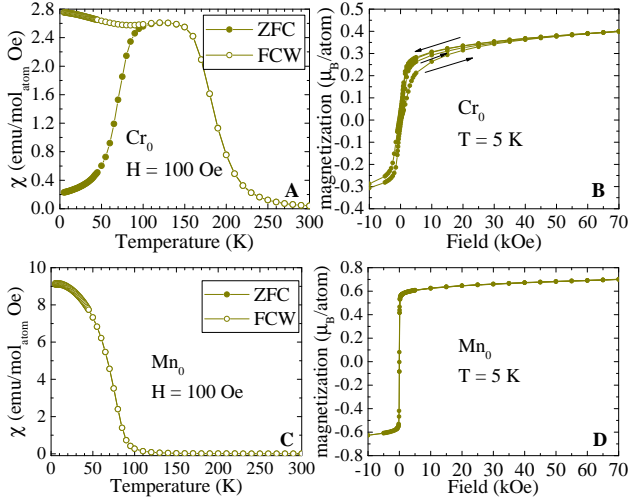


Figure 2. Magnetic susceptibility as a function of temperature for the (A) Cr_0 and (C) Mn_0 samples. Magnetization as a function of applied field for the (B) Cr_0 and (D) Mn_0 samples. Magnetization data for Cr_0 show significant hysteresis, and arrows in panel (B) indicate the direction of the magnetic field sweep for each curve segment. In panel (C), ZFC and FCW curves are difficult to distinguish due to significant overlap, with less than 1% of difference across the entire data range.

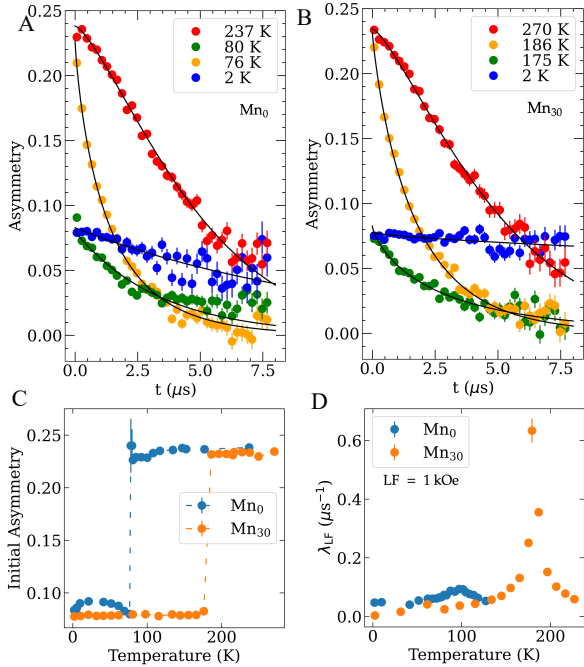


Figure 3. (A, B) Representative zero-field μSR asymmetry spectra for Mn_0 and Mn_{30} , respectively. (C) Temperature dependence of the initial asymmetry at $t = 0$ for both samples, showing a sharp step at the expected transition temperatures. (D) Temperature dependence of the long-time relaxation rate λ_{LF} in an applied longitudinal field of 1 kOe.

4. Discussion

4.1. Modified Curie-Weiss Fitting

Previous work [24] on fitting magnetic susceptibility data for the equiatomic Cantor alloy has revealed the need for a modified Curie-Weiss equation

$$\chi(T) = \chi_0 + \frac{C_m}{T - \theta}, \quad (1)$$

in which C_m is the Curie constant, θ is the Curie-Weiss temperature, and χ_0 is a constant that represents the summation of multiple temperature-independent terms such as Pauli paramagnetism, Van Vleck paramagnetism, Landau diamagnetism, and core diamagnetism [41–45]. One can obtain an effective moment p_{eff} from this fitting using [46]

$$p_{\text{eff}} = 2.82 C_m^{1/2}. \quad (2)$$

In the Cantor alloy, Stoner-enhanced Pauli paramagnetism dominates the χ_0 term, and diamagnetic contributions were predicted to be, at most, 5% of the size of the enhanced Pauli paramagnetism [24]. Van Vleck paramagnetism is present in compounds with a total angular momentum $J = 0$ ground state. In the Cantor alloy, this state may occur in Cr^{2+} and Mn^{3+} , though further work is required to determine whether this mechanism plays a significant role.

Fitting Eq. 1 to the field-cooled susceptibility data produces best fit values of χ_0 , p_{eff} , and θ for 23 different samples. In each case, the data were fit from 300 K down to temperatures just above the highest temperature magnetic ordering transition. The parameters derived from fitting each measured sample are summarized in Table 1. Figure S1 (supplementary material) compares the susceptibility with the fit to Eq. 1 for each sample, demonstrating excellent agreement in almost all cases. Fit parameters are not reported for the two samples that appear to have transitioned to a distinct ferromagnetic ground state, Mn_0 and Cr_0 . For these two samples the fit was unreliable, producing values that were unphysical or depended significantly on the temperature range of the fit.

Several conclusions are immediately apparent on review of Table 1. While the values of the Curie-Weiss temperature, θ , remain close to zero, systematic trends are absent. The temperature independent susceptibility, χ_0 , is consistently of order $\sim 5 \times 10^{-3} \text{ emu mol}_{\text{atom}}^{-1} \text{ Oe}^{-1}$. However, systematic trends in χ_0 are also largely absent, except perhaps in the case of the Ni series. On the other hand, the effective moments, p_{eff} show very clear trends across each substitutional series. These trends are illustrated in Fig. 4a, where it is immediately clear that Cr and Mn suppress the susceptibility, while Fe, Co, and Ni have the opposite effect.

4.2. Element-specific average magnetic moments

Average element-specific magnetic moments can be estimated via a least-squares method using the effective moments in Table 1. Assuming that each element contributes to the total

Source	p_{Cr}	p_{Mn}	p_{Fe}	p_{Co}	p_{Ni}
This work (experiment)	-5.0(1.2)	-3.1(1.2)	3.8(3)	3.2(4)	6.5(7)
This work (DFT)	-0.2(1)	-0.3(1)	1.3(2)	0.7(1)	0.3(4)
Ionization 2+ [39]	4.82	5.82	5.36	4.90	3.12
Ionization 3+ [39]	3.85	4.82	5.82	-	-

Table 2. Effective moments and their uncertainties extracted via least-squares regression compared with empirical effective moments as tabulated in Blundell [39].

effective moment as a linear function of its concentration, the net effective moment of the compound can be expressed as

$$p_{\text{eff}} = \sum_i C_i p_i, \quad (3)$$

in which C_i is the concentration of element i , and p_i is the effective moment of that element. For example, the net effective moment of Ni_{25} could be estimated as

$$0.25 p_{\text{Ni}} + 0.1875(p_{\text{Cr}} + p_{\text{Mn}} + p_{\text{Fe}} + p_{\text{Co}}) = p_{\text{eff}, \text{Ni}_{25}}, \quad (4)$$

and similar equations can be generated for each of the samples for which p_{eff} values are given in Table 1. If one assumes the element-specific magnetic moments are constant across all samples, an over-determined system of equations with only five unknowns is obtained. This set of linear equations can be solved by linear regression to produce best-fit values of the five element-specific magnetic moments. Additional details of the fitting process are described in the Supplementary Material, Sec. S1.

The resulting element-specific moments are tabulated in Table 2. The extracted moments are of order a few μ_B , similar to typical experimental values found for these elements and also of the same order as the Hund's rules values [39]. However, the Cr and Mn moments enter as negative values, suggesting these elements exhibit a strong antiferromagnetic interaction. The solid lines in Fig. 4 are generated for each substitutional series using the moments listed in Table 2 together with Eq. 2. Strikingly, this single set of five element-specific moments produces excellent agreement with the experimentally determined net effective moment across a wide range of compositions.

4.3. Comparison of DFT and experiment

Previous DFT calculations of the equiatomic Cantor alloy suggested a ferrimagnetic ordering at absolute zero [24], where the Fe, Co, and Ni species, and the Cr and Mn species couple ferromagnetically and antiferromagnetically, respectively. In this work, the compositional dependence of the net moment was modeled in parallel to the experimental study, probing the

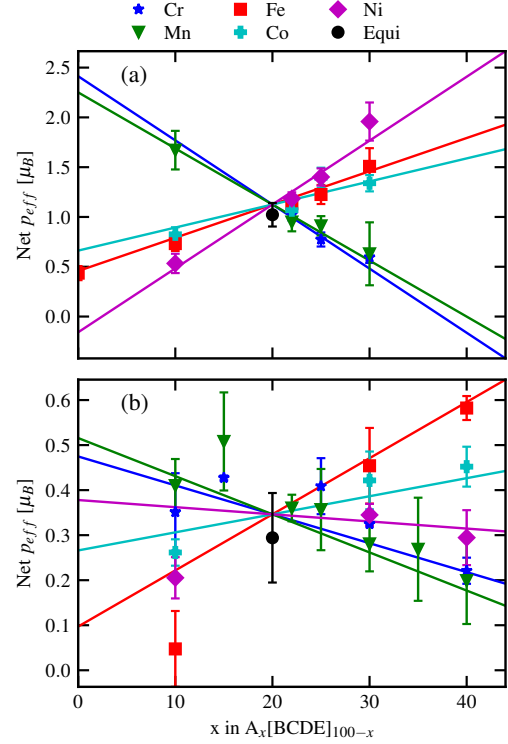


Figure 4. Net magnetic moment vs composition for each series of samples for (a) experimental data and (b) DFT simulations. Each point corresponds to a single sample. Adding Fe, Co, or Ni tends to increase the net moment, while adding Cr or Mn suppresses the net moment. The solid lines represent a model of the data based on element-specific p_{eff} values listed at the bottom of the figure. The element-specific p_{eff} values were determined through a global linear least squares regression of all of the available data as described in the text.

dependence on a per species basis in the same manner as the experimental investigation. These results are shown in Fig. 4(b), where the net moment, as calculated by DFT, is plotted as a function of the variation of each species in the alloy, such that $A_x[\text{BCDE}]_{100-x}$ represents the overall composition. In a similar fashion, a least-square fit is applied to the set of DFT calculated moments to obtain effective local moments of the individual species (see Table 2). Both DFT and experimentally derived element specific moments exhibit consistent signs, i.e., they are in agreement on the ferro- and antiferromagnetic tendency of each species. However, the magnitudes of the effective moments differ. Specifically, they differ on the ferromagnetic strengths of Fe and Ni and on the relative antiferromagnetic strength between Cr and Mn. Notably, DFT calculations predict a weak decrease in net effective moment with increasing Ni concentration, contrary to experimental results. This discord occurs despite the positive moment produced by the linear regression analysis of the DFT moments for Ni. In fact, this behavior can be understood as being due to the rather small Ni moment compared to the moments of Co and Fe, such that increasing Ni concentration proportionally decreases Co and Fe content, which lowers

the overall net moment.

There could be several reasons for the discrepancy in the element specific moments from the analysis of DFT *versus* experimental data. First, the experimental p_{eff} moments were fit to susceptibility data measured in the temperature range of the paramagnetic state, *i.e.*, above any magnetic ordering transition temperature. The DFT p_{eff} moments, on the other hand, were calculated at absolute zero, squarely within the temperature range corresponding to the ferrimagnetic state. Attempting to model the compositional dependence of the paramagnetic state through DFT, however, is not computationally feasible and would likely be subject to errors common to the approximations needed to depict the paramagnetic state in DFT.

Independent of the overall magnetic state, another potential contributing factor for the discrepancy between computationally and experimentally derived moments may be related to thermal expansion. The average volume associated with each atomic lattice site is a factor that has been shown to have significant influence on the local magnetic moment behavior of species in this alloy [47]. As the volume of the lattice site increases, the magnitude of the local moment of each species may also change at different rates. In the case of Mn, Ma *et al.* [47] even showed the net direction of the average Mn spin tended to flip from down to up (or from antiferromagnetic to ferromagnetic) as the atomic volume increases. While the total amount of thermal expansion in the low temperature regime investigated here ($T < 300$ K) is likely small, effects on the local and net moment behavior may still be present.

Billington *et al.* [48] carried out a detailed study of the element specific magnetic properties of the Cantor alloy and certain Cantor alloy variants using a combination of magnetic Compton scattering, x-ray magnetic circular dichroism spectroscopy, and bulk magnetization measurements, noting significant discrepancies between computational and experimental results when examining magnetic moments. However, in compounds where computation and experiment disagreed, computational moments were much larger than experimental ones. For instance, they measured a net moment of $0.008\mu_{\text{B}}$ in a SQUID magnetometer for the equiatomic Cantor alloy, while different theoretical calculations predicted moments between 0.4 and $0.9\mu_{\text{B}}$. However, one should note that the small moment reported from SQUID measurements appears to be based on a high field saturation moment, which is similar in magnitude to the typical magnetization observed at 70 KOe (see Fig. 1). Billington *et al.* attributed these discrepancies to the spin-glass behavior observed in the Cantor alloy and/or an unconventional magnetic ground state. Concerning the present study, the fact that effective moments extracted from modified Curie-Weiss fits are large compared to the magnetization at 70 kOe (and large compared to DFT calculated moments) is fully consistent with the picture that the Cantor alloy is a Stoner-enhanced itinerant magnet [24]. Such systems can exhibit very large ratios of the effective moment to the saturation moment [49].

Finally, the moments extracted from our linear regression analysis and tabulated in the first row of Table 2 should not be expected to correspond exactly to element specific moments directly determined via methods such as inelastic x-ray scat-

tering. Rather, they give the overall incremental contribution to the net effective moment as the concentration of one component of the alloy is adjusted. As such, these moments provide a useful guide to efforts to design Cantor alloy variants with specific magnetic properties.

5. Conclusions

Near the equiatomic composition, the Cantor alloy undergoes two transitions, a ferrimagnetic transition at lower temperature and a spin-glass-like transition at higher temperature. While the spin-glass-like transition temperature varies depending on concentration, the ferrimagnetic transition is remarkably stable, occurring at approximately 43 K in all samples in which it appears despite not resulting from an impurity phase [24]. Trends in the magnetic properties are clearest in the Mn samples, in which larger concentrations shift the spin-glass-like transitions to higher temperatures and decrease the net effective moment. In alloys with low concentrations of Cr or Mn, however, the ferrimagnetic transition becomes ferromagnetic.

Fitting the susceptibility of Cantor alloy samples of many different compositions permits the estimation of the magnetic contribution from each constituent element by assuming a linear contribution from each. This analysis reveals that larger concentrations of ferromagnetic elements Fe, Co, and Ni increase the net effective magnetic moment of the Cantor alloy, while increased quantities of antiferromagnetic elements Cr and Mn decrease the net effective moment. The effective magnetic moments extracted via this process provide a road map facilitating a fine level of control over the magnetic moment of the Cantor alloy by varying its composition. Furthermore, similar regression analyses of data for a variety of chemically substituted samples could be extended to a wider range of high-entropy materials to provide similar insight into the composition dependence of a other properties.

6. Declaration of Competing Interest

The authors declare that they have no known competing financial interests or personal relationships that could have appeared to influence the work reported in this paper.

7. Acknowledgments

T.A.E. and M.W.M. acknowledge support from NSF DMR-1708410. Synthesis and characterization facilities at the University of Florida were developed under support from NSF-CAREER 1453752 (J.J.H.). B.A.F. and E.Z. acknowledge support from the College of Physical and Mathematical Sciences at Brigham Young University and also thank the scientific staff at the Centre for Molecular and Materials Science at TRIUMF, particularly Dr. Gerald Morris, for support during the muon spin relaxation experiment. A portion of this work was performed at the National High Magnetic Field Laboratory, which is supported by the National Science Foundation Cooperative Agreement No. DMR-1644779 and the State of Florida. The

authors acknowledge the staff of the Nano Research Facility at University of Florida for their assistance and guidance in acquiring SEM and XRD data.

The computational work was performed, in part, at the Center for Integrated Nanotechnologies, an Office of Science User Facility operated for the U.S. Department of Energy. Sandia National Laboratories is a multimission laboratory managed and operated by National Technology & Engineering Solutions of Sandia, LLC, a wholly owned subsidiary of Honeywell International Inc., for the U.S. Department of Energy's National Nuclear Security Administration under contract DE-NA0003525. This paper describes objective technical results and analysis. Any subjective views or opinions that might be expressed in the paper do not necessarily represent the views of the U.S. Department of Energy or the United States Government.

References

- [1] Brian Cantor, K. B. Kim, and Paul J. Warren. Novel Multicomponent Amorphous Alloys. *Journal of Metastable and Nanocrystalline Materials*, 13:27–32, 2002. URL <https://dx.doi.org/10.4028/www.scientific.net/JMN.13.27>.
- [2] J.-W. Yeh, S.-K. Chen, S.-J. Lin, J.-Y. Gan, T.-S. Chin, T.-T. Shun, C.-H. Tsau, and S.-Y. Chang. Nanostructured High-Entropy Alloys with Multiple Principal Elements: Novel Alloy Design Concepts and Outcomes. *Advanced Engineering Materials*, 6(5):299–303, 2004. URL <https://dx.doi.org/10.1002/adem.200300567>.
- [3] G. S. Firstov, T. A. Kosorukova, Yu. N. Koval, and V. V. Odnosum. High Entropy Shape Memory Alloys. *Materials Today: Proceedings*, 2:S499–S503, 2015. URL <https://dx.doi.org/10.1016/j.matpr.2015.07.335>.
- [4] Chih-Hsuan Chen and Yue-Jin Chen. Shape memory characteristics of $(\text{TiZrHf})_{50}\text{Ni}_{25}\text{Co}_{10}\text{Cu}_{15}$ high entropy shape memory alloy. *Scripta Materialia*, 162:185–189, 2019. URL <https://dx.doi.org/10.1016/j.scriptamat.2018.11.023>.
- [5] Kapil Motla, Arushi, Pavan K. Meena, and R. P. Singh. Boron based new high entropy alloy superconductor $\text{Mo}_{0.11}\text{W}_{0.11}\text{V}_{0.11}\text{Re}_{0.34}\text{B}_{0.33}$. *arXiv:2201.03300 [cond-mat]*, 2022. arXiv: 2201.03300.
- [6] B. Cantor, I. T. H. Chang, P. Knight, and A. J. B. Vincent. Microstructural development in equiatomic multicomponent alloys. *Materials Science and Engineering: A*, 375-377:213–218, 2004. URL <https://dx.doi.org/10.1016/j.msea.2003.10.257>.
- [7] F. Otto, A. Dlouhý, Ch. Somsen, H. Bei, G. Eggeler, and E. P. George. The influences of temperature and microstructure on the tensile properties of a CoCrFeMnNi high-entropy alloy. *Acta Materialia*, 61(15):5743–5755, 2013. URL <https://dx.doi.org/10.1016/j.actamat.2013.06.018>.
- [8] Mathilde Laurent-Brocq, Alfiya Akhatova, Loïc Perrière, Siham Chebini, Xavier Sauvage, Eric Leroy, and Yannick Champion. Insights into the phase diagram of the CrMnFeCoNi high entropy alloy. *Acta Materialia*, 88:355–365, 2015. URL <https://dx.doi.org/10.1016/j.actamat.2015.01.068>.
- [9] Min Ji Jang, S. Praveen, Hyun Je Sung, Jae Wung Bae, Jongun Moon, and Hyoung Seop Kim. High-temperature tensile deformation behavior of hot rolled CrMnFeCoNi high-entropy alloy. *Journal of Alloys and Compounds*, 730:242–248, 2018. URL <https://dx.doi.org/10.1016/j.jallcom.2017.09.293>.
- [10] Jeoung Han Kim, Ka Ram Lim, Jong Woo Won, Young Sang Na, and Hyoung-Seop Kim. Mechanical properties and deformation twinning behavior of as-cast CoCrFeMnNi high-entropy alloy at low and high temperatures. *Materials Science and Engineering: A*, 712:108–113, 2018. URL <https://dx.doi.org/10.1016/j.msea.2017.11.081>.
- [11] Seong-Woong Kim and Jeoung Han Kim. In-situ observations of deformation twins and crack propagation in a CoCrFeNiMn high-entropy alloy. *Materials Science and Engineering: A*, 718:321–325, 2018. URL <https://dx.doi.org/10.1016/j.msea.2018.01.121>.
- [12] X.F. Wang, Y. Zhang, F. Qiao, and G.L. Chen. Novel microstructure and properties of multicomponent CoCrCuFeNiTi alloys. *Intermetallics*, 15(3):357–362, 2007. URL <https://dx.doi.org/10.1016/j.intermet.2006.08.005>.
- [13] K.B. Zhang, Z.Y. Fu, J.Y. Zhang, J. Shi, W.M. Wang, H. Wang, Y.C. Wang, and Q.J. Zhang. Annealing on the structure and properties evolution of the CoCrFeNiCuAl high-entropy alloy. *Journal of Alloys and Compounds*, 502(2):295–299, 2010. URL <https://dx.doi.org/10.1016/j.jallcom.2009.11.104>.
- [14] Yih-Farn Kao, Swe-Kai Chen, Ting-Jie Chen, Po-Chou Chu, Jien-Wei Yeh, and Su-Jien Lin. Electrical, magnetic, and Hall properties of AlxCoCrFeNi high-entropy alloys. *Journal of Alloys and Compounds*, 509(5):1607–1614, 2011. URL <https://dx.doi.org/10.1016/j.jallcom.2010.10.210>.
- [15] M. S. Lucas, L. Mauger, J. A. Muñoz, Yuming Xiao, A. O. Sheets, S. L. Semiatin, J. Horwath, and Z. Turgut. Magnetic and vibrational properties of high-entropy alloys. *Journal of Applied Physics*, 109(7):07E307, 2011. URL <https://dx.doi.org/10.1063/1.3538936>.
- [16] S. Singh, N. Wanderka, K. Kiefer, S. Siemensmeyer, and J. Banhart. Effect of decomposition of the Cr-Fe-Co rich phase of AlCoCrCuFeNi high entropy alloy on magnetic properties. *Ultramicroscopy*, 111(6):619–622, 2011. URL <https://dx.doi.org/10.1016/j.ultramic.2010.12.001>.
- [17] Liang Liu, Jian Bo Zhu, Jian Chen Li, and Qing Jiang. Microstructure and Magnetic Properties of FeNiCuMnTiSnx High Entropy Alloys. *Advanced Engineering Materials*, 14(10):919–922, 2012. URL <https://dx.doi.org/10.1002/adem.201200104>.
- [18] S.G. Ma and Y. Zhang. Effect of Nb addition on the microstructure and properties of AlCoCrFeNi high-entropy alloy. *Materials Science and Engineering: A*, 532:480–486, 2012. URL <https://dx.doi.org/10.1016/j.msea.2011.10.110>.
- [19] Kuibao Zhang and Zhengyi Fu. Effects of annealing treatment on properties of CoCrFeNiTiAlx multi-component alloys. *Intermetallics*, 28:34–39, 2012. URL <https://dx.doi.org/10.1016/j.intermet.2012.03.059>.
- [20] Ming-Hung Tsai. Physical Properties of High Entropy Alloys. *Entropy*, 15(12):5338–5345, 2013. URL <https://dx.doi.org/10.3390/e15125338>.
- [21] Yong Zhang, TingTing Zuo, YongQiang Cheng, and Peter K. Liaw. High-entropy Alloys with High Saturation Magnetization, Electrical Resistivity and Malleability. *Scientific Reports*, 3(1):1455, 2013. URL <https://dx.doi.org/10.1038/srep01455>.
- [22] Zhaoyuan Leong, Jan S. Wróbel, Sergei L. Dudarev, Russell Goodall, Iain Todd, and Duc Nguyen-Manh. The effect of electronic structure on the phases present in high entropy alloys. *Scientific Reports*, 7(1):39803, 2017. URL <https://dx.doi.org/10.1038/srep39803>.
- [23] Tingting Zuo, Michael C. Gao, Lizhi Ouyang, Xiao Yang, Yongqiang Cheng, Rui Feng, Shuying Chen, Peter K. Liaw, Jeffrey A. Hawk, and Yong Zhang. Tailoring magnetic behavior of CoFeMnNi_x ($x = \text{Al, Cr, Ga, and Sn}$) high entropy alloys by metal doping. *Acta Materialia*, 130:10–18, 2017. URL <https://dx.doi.org/10.1016/j.actamat.2017.03.013>.
- [24] Timothy A. Elmslie, Jacob Startt, Sujeily Soto-Medina, Yang Yang, Keke Feng, Ryan E. Baumbach, Emma Zappala, Gerald D. Morris, Benjamin A. Frandsen, Mark W. Meisel, Michele V. Manuel, Rémi Dingreville, and James J. Hamlin. Magnetic properties of equiatomic CrMnFeCoNi . *Phys. Rev. B*, 106:014418, Jul 2022. doi: 10.1103/PhysRevB.106.014418. URL <https://link.aps.org/doi/10.1103/PhysRevB.106.014418>.
- [25] K. Jin, B. C. Sales, G. M. Stocks, G. D. Samolyuk, M. Daene, W. J. Weber, Y. Zhang, and H. Bei. Tailoring the physical properties of Ni-based single-phase equiatomic alloys by modifying the chemical complexity. *Scientific Reports*, 6(1):20159, 2016. URL <https://dx.doi.org/10.1038/srep20159>. Number: 1 Publisher: Nature Publishing Group.
- [26] Oldřich Schneeweiss, Martin Friák, Marie Dudová, David Holec, Mojmír Šob, Dominik Krieger, Václav Holý, Premysl Beran, Easo P. George, Jörg Neugebauer, and Antonín Dlouhý. Magnetic properties of the CrMnFeCoNi high-entropy alloy. *Physical Review B*, 96(1):014437, 2017. URL <https://dx.doi.org/10.1103/PhysRevB.96.014437>.
- [27] J. Kamarád, M. Friák, J. Kaštil, O. Schneeweiss, M. Šob, and A. Dlouhý. Effect of high pressure on magnetic properties of CrMnFeCoNi high en-

- tropy alloy. *Journal of Magnetism and Magnetic Materials*, 487:165333, 2019. URL <https://dx.doi.org/10.1016/j.jmmm.2019.165333>.
- [28] B. Schuh, F. Mendez-Martin, B. Völker, E.P. George, H. Clemens, R. Pippan, and A. Hohenwarter. Mechanical properties, microstructure and thermal stability of a nanocrystalline CoCrFeMnNi high-entropy alloy after severe plastic deformation. *Acta Materialia*, 96:258–268, 2015. URL <https://dx.doi.org/10.1016/j.actamat.2015.06.025>.
- [29] F. Otto, A. Dlouhý, K. G. Pradeep, M. Kuběnová, D. Raabe, G. Eggeler, and E. P. George. Decomposition of the single-phase high-entropy alloy CrMnFeCoNi after prolonged anneals at intermediate temperatures. *Acta Materialia*, 112:40–52, 2016. URL <https://dx.doi.org/10.1016/j.actamat.2016.04.005>.
- [30] Y. J. Li, A. Savan, A. Kostka, H. S. Stein, and A. Ludwig. Accelerated atomic-scale exploration of phase evolution in compositionally complex materials. *Materials Horizons*, 5(1):86–92, 2018. URL <https://dx.doi.org/10.1039/C7MH00486A>.
- [31] Adrian D. Hillier, Stephen J. Blundell, Iain McKenzie, Izumi Umegaki, Lei Shu, Joseph A. Wright, Thomas Prokscha, Fabrice Bert, Koichiro Shimomura, Adam Berlie, Helena Alberto, and Isao Watanabe. Muon spin spectroscopy. *Nat. Rev. Methods Primers*, 2:4, 2022. doi: 10.1038/s43586-021-00089-0.
- [32] K. Alec Petersen, Jared Black, and Benjamin A. Frandsen. BEAMS: Basic and Effective Analysis for Muon Spin Spectroscopy, 2021.
- [33] G. Kresse and J. Hafner. Ab initio molecular dynamics for liquid metals. *Phys. Rev. B*, 47(1):558–561, 1993. doi: <https://doi.org/10.1103/PhysRevB.47.558>.
- [34] G. Kresse and J. Hafner. Ab initio molecular-dynamics simulation of the liquid-metamorphous- semiconductor transition in germanium. *Phys. Rev. B*, 49(20):14251–14269, 1994. doi: <https://doi.org/10.1103/PhysRevB.49.14251>.
- [35] G. Kresse. Ab initio molecular dynamics for liquid metals. *J. Non-Cryst. Solids*, 192-193:222–229, 1995. doi: [https://doi.org/10.1016/0022-3093\(95\)00355-X](https://doi.org/10.1016/0022-3093(95)00355-X).
- [36] P.E. Blochl. Projector augmented-wave method. *Phys. Rev. B*, 50(24):17979, 1994. doi: <https://doi.org/10.1103/PhysRevB.50.17953>.
- [37] G. Kresse and D. Joubert. From ultrasoft pseudopotentials to the projector augmented-wave method. *Phys. Rev. B*, 59(3):1758–1775, 1999. doi: <https://doi.org/10.1103/PhysRevB.59.1758>.
- [38] J.P. Perdew, K. Burke, and M. Ernzerhof. Generalized gradient approximation made simple. *Phys. Rev. Lett.*, 77(18):3865–3868, 1996. doi: <https://doi.org/10.1103/PhysRevLett.77.3865>.
- [39] Stephen Blundell. *Magnetism in Condensed Matter*. Oxford University Press, Oxford, New York, 2001. ISBN 0-19-850592-2.
- [40] Y.J. Uemura. μ SR relaxation functions in magnetic materials. In S.L. Lee, R. Cywinski, and S.H. Kilcoyne, editors, *Muon Science: Muons in Physics, Chemistry and Materials*. Taylor & Francis, New York, 1999.
- [41] Laxman N Mulay, Edward A Boudreaux, et al. *Theory and applications of molecular diamagnetism*. Wiley, 1976.
- [42] G. Cao, J. E. Crow, R. P. Guertin, P. F. Henning, C. C. Homes, M. Strongin, D. N. Basov, and E. Lochner. Charge density wave formation accompanying ferromagnetic ordering in quasi-one-dimensional BaIrO₃. *Solid State Communications*, 113(11):657–662, 2000. URL [https://dx.doi.org/10.1016/S0038-1098\(99\)00532-3](https://dx.doi.org/10.1016/S0038-1098(99)00532-3).
- [43] H. Kaldarar, E. Royanian, H. Michor, G. Hilscher, E. Bauer, A. Griбанov, D. Shtepa, P. Rogl, A. Grytsiv, Y. Seropegin, and S. Nesterenko. Thermal and electronic properties of CePd₃In₂. *Physical Review B*, 79(20):205104, 2009. URL <https://dx.doi.org/10.1103/PhysRevB.79.205104>.
- [44] Tadeusz Groń, Andrzej W. Pacyna, and E. Malicka. Influence of Temperature Independent Contribution of Magnetic Susceptibility on the Curie-Weiss Law. *Solid State Phenomena*, 170:213–218, 2011. URL <https://dx.doi.org/10.4028/www.scientific.net/SSP.170.213>.
- [45] M. M. Markina, B. V. Mill, E. A. Zvereva, A. V. Ushakov, S. V. Streltsov, and A. N. Vasiliev. Magnetic phase diagram and first-principles study of Pb₃TeCo₃V₂O₁₄. *Physical Review B*, 89(10):104409, 2014. URL <https://dx.doi.org/10.1103/PhysRevB.89.104409>.
- [46] Mike McElfresh. *Fundamentals of Magnetism and Magnetic Measurements*. Quantum Design, 1994.
- [47] D. Ma, B. Grabowski, F. Körmann, J. Neugebauer, and D. Raabe. Ab initio thermodynamics of the coCrFeMnNi high entropy alloy: Importance of entropy contributions beyond the configurational one. *Acta Mat.*, 100:90–97, 2015. ISSN 1359-6454. doi: 10.1016/j.actamat.2015.08.050. URL <https://doi.org/10.1016/j.actamat.2015.08.050>.
- [48] D. Billington, A. D. N. James, E. I. Harris-Lee, D. A. Lagos, D. O’Neill, N. Tsuda, K. Toyoki, Y. Kotani, T. Nakamura, H. Bei, S. Mu, G. D. Samolyuk, G. M. Stocks, J. A. Duffy, J. W. Taylor, S. R. Giblin, and S. B. Dugdale. Bulk and element-specific magnetism of medium-entropy and high-entropy Cantor-Wu alloys. *Physical Review B*, 102(17):174405, 2020. URL <https://dx.doi.org/10.1103/PhysRevB.102.174405>.
- [49] P. Rhodes, E. P. Wohlfarth, and Harry Jones. The effective Curie-Weiss constant of ferromagnetic metals and alloys. *Proceedings of the Royal Society of London. Series A. Mathematical and Physical Sciences*, 273(1353):247–258, May 1963. doi: 10.1098/rspa.1963.0086. URL <https://royalsocietypublishing.org/doi/abs/10.1098/rspa.1963.0086>.

Supplementary Material: Tuning the Magnetic Properties of the CrMnFeCoNi Cantor Alloy

Timothy A. Elmslie^a, Jacob Startt^b, Yang Yang^c, Sujeily Soto-Medina^c, Emma Zappala^d,
Mark W. Meisel^{a,c}, Michele V. Manuel^c, Benjamin A. Frandsen^d, Rémi Dingreville^b, James J. Hamlin^a

^a*Department of Physics, University of Florida, Gainesville, FL 32611-8440, USA*

^b*Center for Integrated Nanotechnologies, Sandia National Laboratories, Albuquerque, NM, 87185, USA*

^c*Department of Materials Science and Engineering, University of Florida, Gainesville, FL 32611-6400, USA*

^d*Department of Physics and Astronomy, Brigham Young University, Provo, UT 84602, USA*

^e*National High Magnetic Field Laboratory, University of Florida, Gainesville, Florida 32611-8440, USA*

S1. Compositional and Structural Analysis

The representative samples Ni₁₀ and Cr₃₀ were investigated using SEM and XRD. In the Ni₁₀ sample, micro-sized pores were found, which are considered formed during casting. Using BSE and EDX, a small number of particles were detected and identified as oxides rich in Cr and Mn. The crystal of the sample was determined as FCC single phase according to the XRD shown in Fig. S1. No peak corresponding to the oxide particles was found in the XRD pattern. This kind of (Cr, Mn)-rich particle was reported in previous studies [? ? ?], but was not able to be detected using XRD. The investigated properties were unlikely to be affected by these inclusions due to the small volume fraction thereof. The compositions of the anneal Ni₁₀ was measured using EDX as shown in Table S1.

Table S1: Compositions of the anneal Ni₁₀ measured by SEM-EDX.

Element	at.%
Cr	22(1)
Mn	22.1(2)
Fe	22.9(1)
Co	22.9(9)
Ni	9.7(3)

Figure S1 shows SEM-BSE and XRD measurements on the samples Ni₁₀ and Cr₃₀. In the Cr₃₀ sample, a secondary phase was observed in the BSE image with lighter contrast. This secondary phase was inhomogeneously distributed along the grain boundaries, pores and inclusions. The composition of this phase is characterized rich in Cr than the matrix using EDX as shown in Table S2. However, no peak was found in the XRD pattern corresponding to the second phase.

Email address: jhamlin@uf1.edu (James J. Hamlin)

Table S2: Compositions of the second phase and matrix in anneal Cr₃₀ measured by SEM-EDX.

Element at.%	Precipitate	Matrix
Cr	46.5(1)	29.5(1)
Mn	14.3(1)	17.9(1)
Fe	15.5(1)	18(1)
Co	14.7(1)	17.4(1)
Ni	8.9(1)	17.2(1)

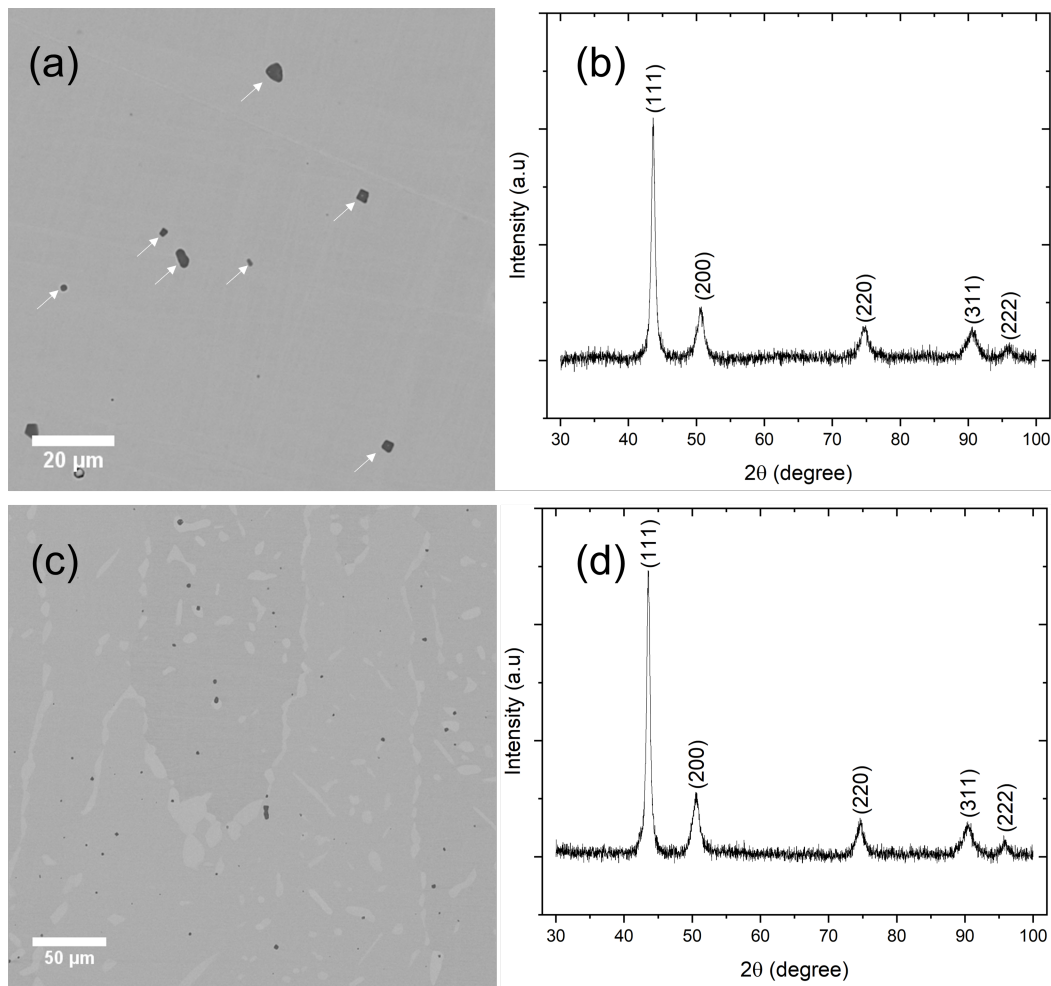


Figure S1: (a) SEM-BSE image of the anneal Ni₁₀ contains small number of oxide particles indicated by arrows. The compositions of the inclusions were found rich in Cr and Mn using EDX. (b) The crystal structure of the Ni₁₀ was found FCC single phase using XRD. (c) SEM-BSE image of the anneal Cr₃₀ showed oxide particles, pores and the second phase with lighter contrast. (d) The second phase was not detected using XRD, which showed FCC single phase.

S2. Modified Curie-Weiss Fits

The χ_0 , p_{eff} , and Θ values displayed in Table 1 (main text) were obtained by fitting a modified Curie-Weiss equation to experimental susceptibility data. We used the `scipy.optimize.curve_fit` non-linear least squares fitting function from the `scipy` library to perform the fits. The datasets and corresponding fits for each fitted sample are compared in Fig. S2.

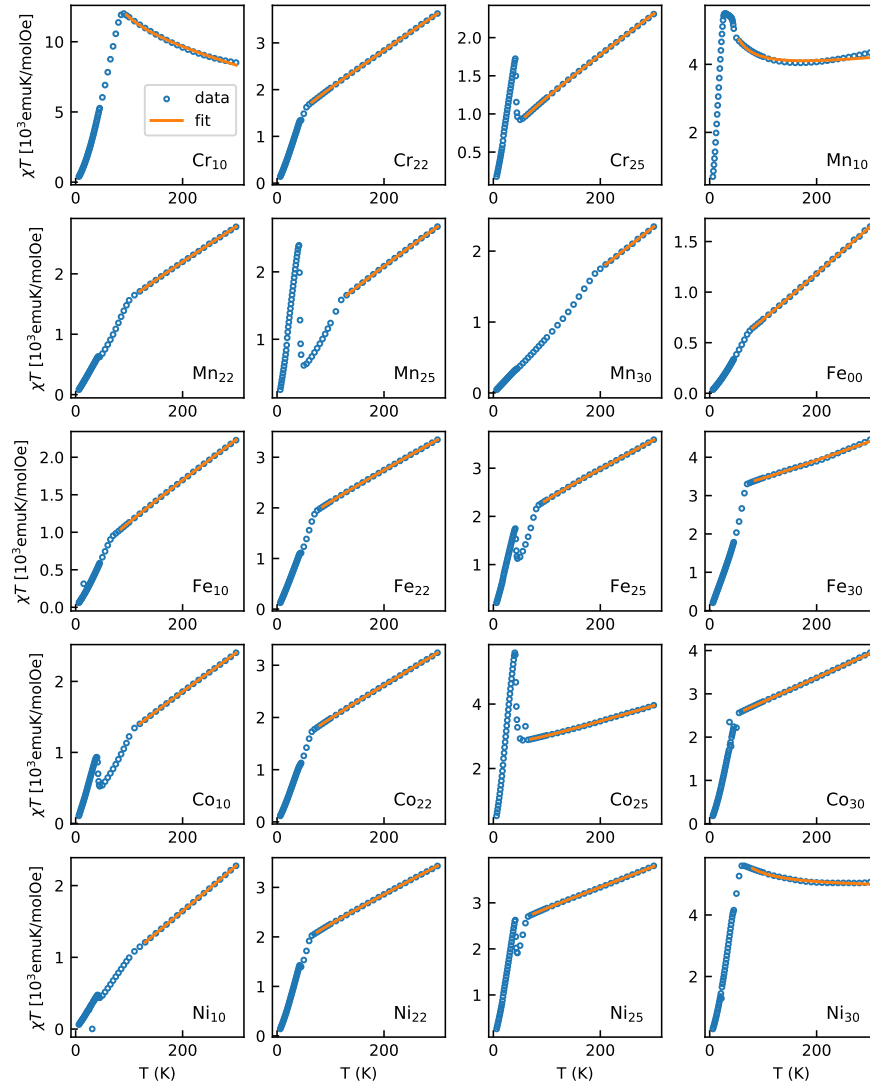


Figure S2: Modified Curie-Weiss fits shown in orange compared with experimental data shown in blue for a characteristic selection of measured samples. Data are plotted as susceptibility times temperature versus temperature for greater readability across the entire measured temperature range.

S3. Least-squares solution for element-specific magnetic moments

As described in the main text we construct a system of equations (Eq. 3 in the main text) using the measured effective moments and known elemental concentrations for each sample. The unknowns in these equations are the element-specific magnetic moments. It is possible to write this equation for each sample. We then solved the linear matrix equation using the `numpy.linalg.lstsq` function from the `numpy` library. Since the system of equations is over-determined, we obtain best fit values for the element-specific moments, rather than an exact solution.

S3.1. Omitted samples

Three samples that are included in Table 1 (main text) were omitted from this analysis. These included the Cr_0 , Cr_{10} , and Mn_0 samples. After omitting these samples, data for 23 samples remained. This included four distinct samples of the equiatomic composition. In the case of Cr_0 and Mn_0 , fitting with the modified Curie-Weiss equation (Eq. 1 main text), produced unreliable results that depended on the temperature range of the fit or produced unphysical large negative values of χ_0 . This is presumably related to transition to a more strongly ferromagnetic state in those materials and, in the case of Cr_0 the fact that a very limited temperature range above the Curie temperature is available for fitting.

The Cr_{10} magnetization data was relatively well fit by the modified Curie-Weiss equation as shown in the top row of Fig. S2. However, the fit produced an anomalously large $p_{\text{eff}} \sim 3\mu_B$. Including the Cr_{10} data in the global least squares solution produced overall poor agreement. We found that leaving out the Cr_{10} data reduced the overall residual of the fit by nearly a factor of four, while leaving out any other data for any other sample had a minimal effect on the residual. We therefore omitted the Cr_{10} datapoint from the fit. The reason for the poor agreement of the Cr_{10} point with the rest of the data is likely connected with the fact that this sample is on the verge of a transition to the more ferromagnetic state that is observed in Cr_0 . We are currently further investigating the transition to ferromagnetism in the Cr-poor series.

S3.2. Uncertainty estimates

The `numpy.linalg.lstsq` function does not provide a straightforward means of taking into account the uncertainties in the values of p_{eff} for each sample (left side of Eq. 3 in the main text). In order to generate uncertainty values for the element-specific moments that take into account the uncertainties in the input (p_{eff}) data, we used the following approach:

1. Apply a Gaussian randomization to the values of p_{eff} such that they vary around the best fit value with a standard deviation equal to the uncertainties reported in Table 1 (main text).
2. Solve the resulting linear matrix equation consisting of data on 23 samples to produce a set of element-specific magnetic moments.
3. Repeat steps 1-2 a total of 10^5 times to produce a distribution of element-specific moments. These distributions are shown in Fig. S3
4. The values and uncertainties of the element-specific magnetic moments are then taken from the mean and standard deviations of the resulting distributions.

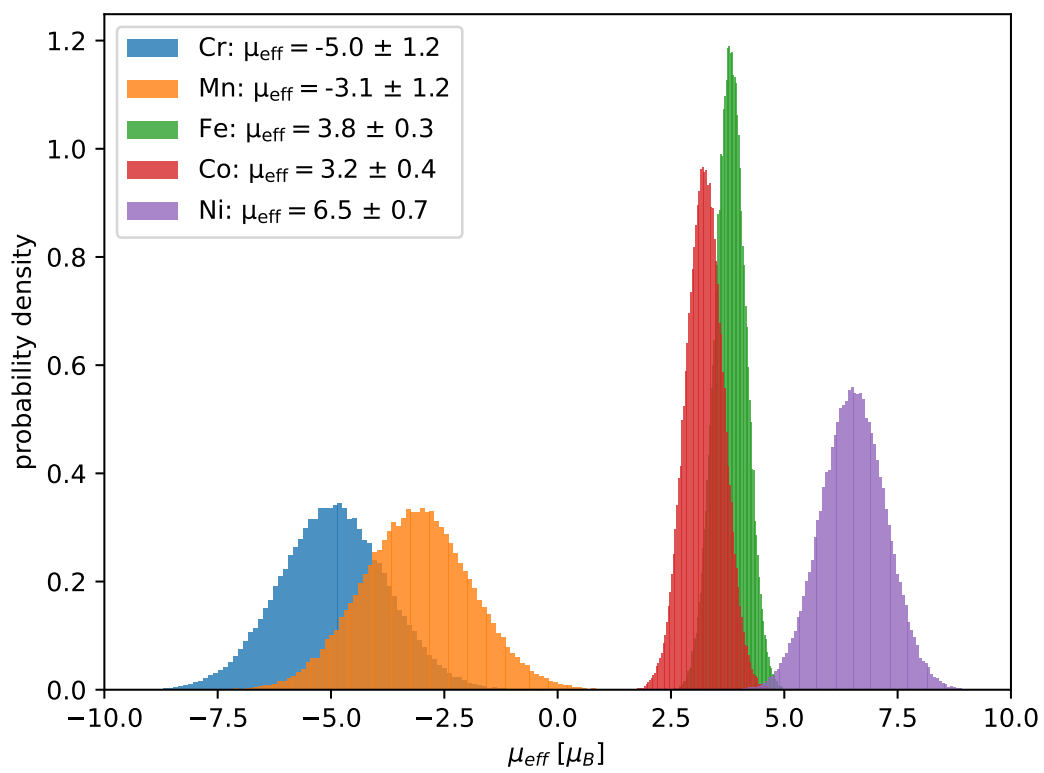


Figure S3: Distribution of element-specific magnetic moments as determined by randomly varying the values of the input ρ_{eff} values. This allows the uncertainty in the values of ρ_{eff} for each sample to be accounted for in determining the uncertainties in the element-specific magnetic moments.